Water Research 209 (2022) 117890

Contents lists available at ScienceDirect

Water Research

journal homepage: www.elsevier.com/locate/watres

Mineralization of cyanides via a novel Electro-Fenton system generating •OH and $•O_2^-$

Lei Tian [a,b], Peng Chen [a], Xun-Heng Jiang [a,b], Li-Sha Chen [a,b], Lin-Lin Tong [c], Hong-Ying Yang [c], Jie-Ping Fan [b], Dai-She Wu [b], Jian-Ping Zou [a,b,*], Sheng-Lian Luo [a]

[a] National-Local Joint Engineering Research Center of Heavy Metals Pollutants Control and Resource Utilization, Nanchang Hangkong University, Nanchang 330063, China
[b] Key Laboratory of Poyang Lake Environment and Resource Utilization, Ministry of Education, School of Resources Environmental and Chemical Engineering, Nanchang University, Nanchang 330031, China
[c] School of Metallurgy, Northeastern University, Shenyang 110819, China

ARTICLE INFO

Keywords:
Advanced oxidation processes
Cyanides
Mineralization
Electro-Fenton
Nitrates

ABSTRACT

Traditional methods of cyanides' (CN^-) mineralization cannot overcome the contradiction between the high alkalinity required for the inhibition of hydrogen cyanide evolution and the low alkalinity required for the efficient hydrolysis of cyanate (CNO^-) intermediates. Thus, in this study, a novel Electro-Fenton system was constructed, in which the free cyanides released from ferricyanide photolysis can be efficiently mineralized by the synergy of •OH and $•O_2^-$. The complex bonds in ferricyanide (100 mL, 0.25 mM) were completely broken within 80 min under ultraviolet radiation, releasing free cyanides. Subsequently, in combination with the heterogeneous Electro-Fenton process, $^•OH$ and $^•O_2^-$ were simultaneously generated and 92.9% of free cyanides were transformed into NO_3^- within 120 min. No low-toxic CNO^- intermediates were accumulated during the Electro-Fenton process. A new conversion mechanism was proposed that CN^- was activated into electron-deficient cyanide radical ($^•CN$) by $^•OH$, and then the $^•CN$ intermediates reacted with $^•O_2^-$ via nucleophilic addition to quickly form NO_3^-, preventing the formation of CNO^- and promoting the mineralization of cyanide. Furthermore, this new strategy was used to treat the actual cyanide residue eluent, achieving rapid recovery of irons and efficient mineralization of cyanides. In conclusion, this study proposes a new approach for the mineralization treatment of cyanide-containing wastewater.

1. Introduction

Cyanides (CN^-) are widely used in numerous industrial processes such as mining, electroplating, coking, etc., due to their characteristic properties for complexing metals such as Au, Ag, Cu, or Fe (Dash et al., 2009a; Kuyucak and Aguado, 2013). As a result, cyanides are often present as complexations with metals in the corresponding wastewaters (Castilla-Acevedo et al., 2020). Although the toxicity of cyanocomplexes is relatively lower than that of free cyanides, these cyanocomplexes can be dissociated under specific severe conditions (such as strong acid, UV radiation, or high temperature), releasing highly toxic hydrogen cyanide (HCN) and causing potential damage to the ecosystem (Johnson, 2015). It is therefore vital to treat cyanides and cyanocomplexes contaminated effluents before their discharge into the environment.

Different treatment technologies such as alkaline chlorination, adsorption, biodegradation, and advanced oxidation processes (AOPs) have been investigated to remove cyanides and cyanocomplexes Akcil, 2003; Dash et al., 2009b; Novak et al., 2013). In general, these technologies have some common drawbacks such as poor treatment efficiency, high cost, and production of low-toxic intermediates (cyanate, CNO^-), which require further treatment to achieve deep mineralization of cyanides and cyanocomplexes. Previous studies have proposed traditional pathways for the cyanides and cyanocomplexes mineralization (as shown in Eqs. (1)–((3)) and have indicated that hydrolysis of CNO^- intermediate is the rate-limiting step for the entire process (Teo and Tan, 1987). However, to prevent the volatilization of highly toxic HCN gas ($pKa = 9.21$), the reaction system must be maintained in a strongly alkaline medium during the process of cyanides and

* Corresponding author at: National-Local Joint Engineering Research Center of Heavy Metals Pollutants Control and Resource Utilization, Nanchang Hangkong University, Nanchang 330063, P. R. China.
E-mail address: zjp_112@126.com (J.-P. Zou).

https://doi.org/10.1016/j.watres.2021.117890
Received 22 September 2021; Received in revised form 17 November 2021; Accepted 19 November 2021
Available online 24 November 2021

cyanocomplexes removal. On the other hand, the generated CNO^- is a weak acid salt and cannot be hydrolyzed to form NH_4^+/NH_3 under strongly basic conditions, which makes the mineralization of cyanides and cyanocomplexes very difficult. Based on this case, Koo et al. (2021) proposed a photoelectrochemical system to generate hypochlorites (OCl^-) and convert CN^- to N_2 under weakly alkaline conditions (pH = 9.6). The generated CNO^- was slowly hydrolyzed under a predefined alkalescence and then reacted with OCl^- to generate N_2. Furthermore, Xiao et al. (2019) explored a photoelectrochemical system incorporating Cl^- in the electrolyte (PEC-Cl) and with WO_3 as the photoanode to treat Cu-cyanide complexes at pH 8. The chlorine radicals ($ClO^•$ and/or $Cl^•$) were dedicated to the mineralization of Cu-cyanide complexes. Nevertheless, these methods are inefficient and are accompanied by significant risks, which could result in the formation of HCN under weakly alkaline conditions. Therefore, there is an urgent need to develop a novel strategy to effectively achieve cyanides and cyanocomplexes mineralization without the risk of HCN evolution.

$$CN^- + \text{Oxidant} \rightarrow CNO^- \quad (1)$$

$$CNO^- + 2H_2O \rightarrow NH_3/NH_4^+ + HCO_3^-/CO_3^{2-} \quad (2)$$

$$NH_3/NH_4^+ + \text{Oxidant} \rightarrow NO_3^-/N_2 \quad (3)$$

Generally, the conversion between CN^- and CNO^- was considered as a one-step reaction mediated by active species. In fact, CN^- could be transformed into various unstable intermediates during the oxidation process and finally be converted to CNO^-. For instance, Zhao et al. (2015) reported that the electron-deficient cyanide radical ($^•CN$) could be produced in the oxidation process of cyanide by $^•OH$ or photo-generated holes (h^+). Subsequently, $^•CN$ would be self-quenched and further hydrolyzed into CNO^- Eqs. (4)–((6)). Based on the reported results, we can assume that the formation of CNO^- could be avoided to the extent possible if the $^•CN$ intermediate was quickly expended but not self-quenched. Superoxide radical ($^•O_2^-$) is a unique species with a low redox potential (-0.81 V vs. standard hydrogen electrode at pH 7 and 20 ℃) (Ding et al., 2014). It is a strong electron donor and could undergo nucleophilic addition with some electron-deficient intermediates such as phenoxyl radical and activated NO (NO^+) (Chen et al., 2018; Ma et al., 2020; Mitchell et al., 2013). Besides, $^•O_2^-$ possesses good stability under alkaline conditions and its half-life ranges from microseconds to minutes (McDowell et al., 1983), which is well suited for cyanide removal. Moreover, under alkaline conditions, the presence of a large amount of OH^- can consumingly inhibit the quenching reaction between $^•OH$ and $^•O_2^-$. Theoretically, in case of co-existence of $^•O_2^-$ and $^•OH$, CN^- would preferably be deprived of an electron by $^•OH$ to form electron-deficient $^•CN$ due to that $^•OH$ (1.8-2.7 V vs. NHE) is a strong electron acceptor and more reactive than $^•O_2^-$ (Luo et al., 2021). Then the generated $^•CN$ could react with $^•O_2^-$ to generate nitrate (NO_3^-). Therefore, we hypothesized that the traditional cyanide mineralization pathway would be overturned if specific $^•OH$ and $^•O_2^-$ could be introduced simultaneously into the cyanide removal process.

$$^•OH + CN^- \rightarrow OH^- + {}^•CN \quad (4)$$

$$2{}^•CN \rightarrow (CN)_2 \quad (5)$$

$$(CN)_2 + 2OH^- \rightarrow CN^- + CNO^- + H_2O \quad (6)$$

Electro-Fenton (EF) system, as a promising AOPs, can accurately produce $^•OH$ and $^•O_2^-$ simultaneously *in situ* by transition metal ion/transition metal oxide and electro-generated H_2O_2 at the cathode Eqs. (7)–((9)). Compared with photocatalysis and other AOPs, EF system has the advantages of easy operation, low cost, and precise control for the generation of specific active species (Zhao et al., 2016; Zhang et al, 2020). However, the conventional homogeneous/heterogeneous EF systems, restricted to secondary pollution, impractically narrow pH range, difficult recovery of catalyst, and poor stability, aren't appropriate for the strongly alkaline cyanide-containing wastewater. Recently, the electrocatalysis coupled with AOPs technology, in which the variable-valence transition metal oxide was immobilized into the anode, has been developed by our group and testified to be an efficient strategy to overcome the above problems (Zou et al., 2018; Zhu et al., 2020). More importantly, simple potential regulation in this novel system could accurately control the type and the concentrations of active species. In addition, among numerous transition metal oxides, manganese oxides (such as MnO_2, Mn_2O_3, Mn_3O_4) are the more excellent heterogeneous Fenton catalyst compared with iron oxides or cobalt oxides due to their higher catalytic activity and higher stability over a wide pH range (Tian et al., 2019; He et al., 2020). Therefore, we speculate the effective mineralization of cyanides could be achieved by the novel EF system with manganese oxides as the anode.

$$O_2 + e^- \rightarrow {}^•O_2^- \quad (7)$$

$$^•O_2^- + e^- + 2H_2O \rightarrow H_2O_2 + 2OH^- \quad (8)$$

$$\equiv M(n)/M(n) + H_2O_2 \rightarrow \equiv M(n+1)/M(n+1) + {}^•OH + OH^- \quad (9)$$

To test the hypothesis, this work developed a novel EF system to achieve highly efficient mineralization of cyanides released from the preprocessed photolysis of ferricyanide, the most common cyanocomplexes with a very large stability constant in industrial wastewater. Among the EF system, the manganic oxide (Mn_2O_3/Nickel Foam (NF), i.e., Mn_2O_3 below) anode was combined with the active carbon fiber (ACF) cathode, and specific $^•OH$ and $^•O_2^-$ were generated simultaneously and cyanides were rapidly transferred into NO_3^-. The mechanism of cyanide conversion was studied in detail through batch experiments, characterization and theoretical calculations. Finally, this strategy was used to process the actual cyanide residue eluent (iron: 145.8 mg/L; total cyanide: 437.3 mg/L; free cyanide: 33.4 mg/L) and investigated its feasibility for practical application. The present work develops a novel pathway for efficient mineralization of cyanides to form NO_3^- but not CNO^- and opens a new avenue to invent good technologies for highly efficient treatment of cyanide and cyanocomplexe contaminated effluents.

2. Materials and methods

2.1. Experimental procedures

Photolysis pretreatment: firstly, the photolysis operation to break the complex bonds between iron and cyanide was undertaken in a quartz beaker (150 mL), which contained 100 mL of $K_3Fe(CN)_6$ at a preset concentration of 0.25 mM. The pH value was adjusted to 12.0 by NaOH to prevent the formation of HCN gas. A 300 W Xe lamp (Beijing, Perfect light Inc, China) was used as the source of ultraviolet radiation. The UV light was irradiated from the top of the beaker, and the distance between the light source and the beaker was 5 cm. After a period of photolysis, the solution was filtered to separate the iron precipitate and free cyanide.

Electro-Fenton reaction: then, about 90 mL of free cyanide solution was transferred to an undivided cylindrical glass electrolytic cell (Schematic diagram was provided in Fig. S1 in SI). A Mn_2O_3 anode and an ACF cathode were fixed at a gap of 3 cm in the reactor and connected to a potentiostat (CHI 660E electrochemical workstation (Shanghai, Chenhua, China)). The detailed processes for the preparation of the Mn_2O_3 anode and ACF cathode are available in Text S2. Ag/AgCl was used as the reference electrode. Before the EF reaction, 0.1 M Na_2SO_4 was added to the free cyanide solution to regulate the conductivity. The electrodes were inserted into the solution and held for 1 h under magnetic stirring to establish maximum cyanide adsorption. The immersed area of the electrode was 4.5 cm^2. During the reaction process, samples were taken with syringes at designated time intervals and immediately filtered through 0.45 μm polytetrafluoroethylene (PTFE) membranes. All experiments were conducted three times.

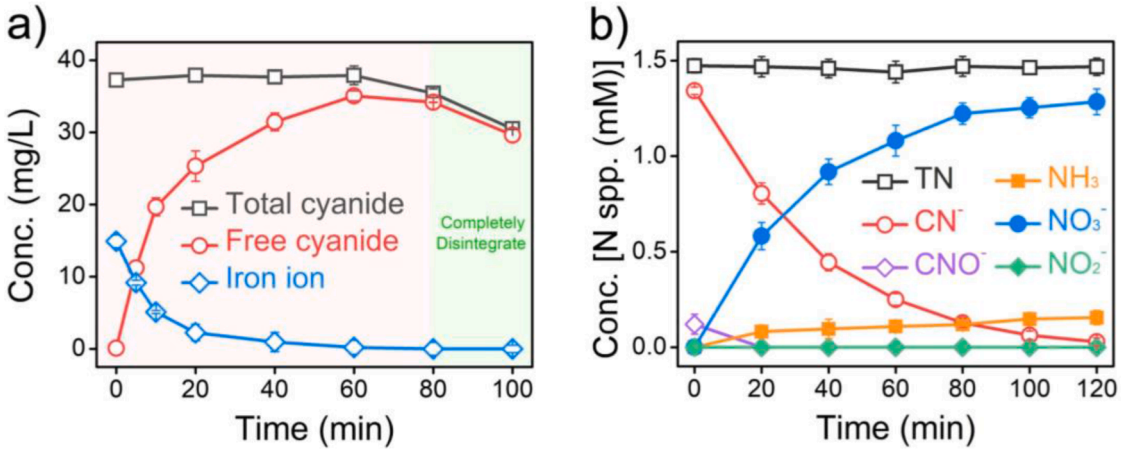

Fig. 1. (a) Species concentration variation under UV irradiation. Reaction conditions: $[Fe(CN)_6^{3-}] = 0.25$ mM, initial pH = 12.0; (b) Nitrogen species concentration variation in the EF system, in which Mn_2O_3 anode was prepared with 3 mM manganese source. Reaction conditions: $[CN^-] = 1.35$ mM, $[Na_2SO_4] = 100$ mM, bias potential = 2.5 V, initial pH = 11.50, T = 298 K.

2.2. Analysis methods

Isonicotinic acid-barbituric acid colorimetry was used for the determination of total cyanide via a UV-vis spectrophotometer (U-3900, Hitachi Ltd, Japan) at the wavelength of 600 nm after distillation (APHA, AWWA, WEF, 2012). The detailed test method is shown in Text S3 in the SI. Free cyanide concentration was determined by the above method without distillation. Cyanate (CNO^-), nitrate (NO_3^-) and nitrite (NO_2^-) concentrations were measured using an ion chromatography system (Dionex-120, Dionex Inc, USA). Ammonia (NH_3/NH_4^+) concentration was analyzed by the Nessler's reagent method. The total nitrogen (TN) concentration was measured by spectrophotometry after its oxidation with potassium persulfate. The dissolved iron concentration was measured using a ConteAA 700 flame atomic absorption spectrophotometer (Analytik Jena, Germany). The concentration of hydrogen peroxide (H_2O_2) was measured by the traditional titration method of cerium sulfate $Ce(SO_4)_2$ using a UV-vis spectrophotometer at the wavelength of 316 nm (Lu et al., 2018). Benzoic acid (BA) and nitrotetrazolium blue chloride (NBT) were used as probes to quantify the generation of $^{\bullet}OH$ and $^{\bullet}O_2^-$ in the EF system (He et al., 2020; Joo et al., 2005). The intermediates of N-tert-butyl-α-phenylnitrone (PBN) were detected by liquid chromatography mass spectrometry (LC-MS, Agilent. 6120, America) equipped with a C18 column and an electrospray ionization source. The spray voltage was 3000 V and the gasification temperature was 350 °C. The mobile phase was acetonitrile-water (70:30, v/v) and the flow rate was 0.4 mL/min. For EPR measurement, 100 μL of the sample was collected from the EF system and immediately mixed with DMPO or BMPO. ESR spectra were obtained on a Bruker A300 spectrometer (Germany). The energy consumption (EC, kWh/m^3) was calculated through Eq. (10).

$$EC = \frac{U \times I \times t \times 1000}{\log(C_0/C_t) \times V} \quad (10)$$

where U is the applied voltage (V), I the average current (A), t the time (h), V the solution volume (L), $\log(C_0/C_t)$ the logarithm of the initial and instant concentrations of the cyanide.

3. Results and discussion

3.1. Photolysis of ferricyanides

Ferricyanides are pertinacious with strong stability constant, second to only to hexacyanocobaltate in all metal-cyanide complexes, and cannot be effectively removed by conventional methods Castilla-Acevedo et al., 2020). As shown in Fig. S3, the non-photolyzed ferricyanide existed tenaciously in the proposed EF system. However, it is reported that ferricyanides are very photosensitive and the complex bonds in ferricyanide could be broken under UV irradiation, releasing free cyanide ligand (Grieken et al., 2005). Therefore, ferricyanide was initially pretreated under Xenon lamp irradiation, and the dissociation path is shown in Fig. S4 in the SI. During the photolysis process, the complexation bonds between iron and cyanide are effectively broken and six cyanide ligands are released one by one. The iron element can precipitate as $Fe(OH)_3$ (Grieken et al., 2005). As shown in Fig. 1a, with irradiation proceeding, the concentration of free cyanide gradually increased, while the concentration of iron ions inversely changed. Besides, the iron ions were precipitated as ferric hydroxide, which could be proved by the color and X-Ray Diffraction of sediment (Fig. S5). Besides, the concentrations of free cyanide and total cyanide began to decrease after 60 min, whereas the free cyanide concentration was markedly lower than the total cyanide concentration. The result indicated that a small amount of ferricyanide still couldn't be broken after 60 min UV irradiation. Moreover, when the irradiation time reached 80 min, the concentration of free cyanide was close to that of total cyanide and there were no dissolved iron ions in the solution, indicating the conversion of cyanocomplexes to free cyanides has been completely accomplished. Excessive UV irradiation could cause water to undergo homolysis (Eq. (11)), producing oxidizing species such as $^{\bullet}OH$ that oxidized free cyanide to cyanate (Eqs. ((2), (3)). Therefore, in order to ensure the complete dissociation of ferricyanide, the ultraviolet irradiation time was set to 80 min.

$$H_2O \rightarrow {}^{\bullet}OH + H^+ + e_{aq}^- \quad (11)$$

3.2. Mineralization of cyanides

The solution of free cyanides (i.e., CN^- below) obtained from the photolysis of ferricyanide was transferred to the EF system. Due to excessive UV radiation, the CN^- ligands of 1.5 mM in 0.25 mM ferricyanide could be slightly oxidized, resulting in the CN^- concentration after photolysis decreasing to 1.35 mM. Thus, the concentration of CN^- was set as 1.35 mM.

Subsequently, the effects of the amount of manganese source in the anode preparation and the bias voltage on CN^- removal were systematically investigated. As can be seen in Table S1 and Fig. S6 in the SI, with the increase in the amount of manganese source in the anode preparation process (1–3 mM), the manganese content on the bulk

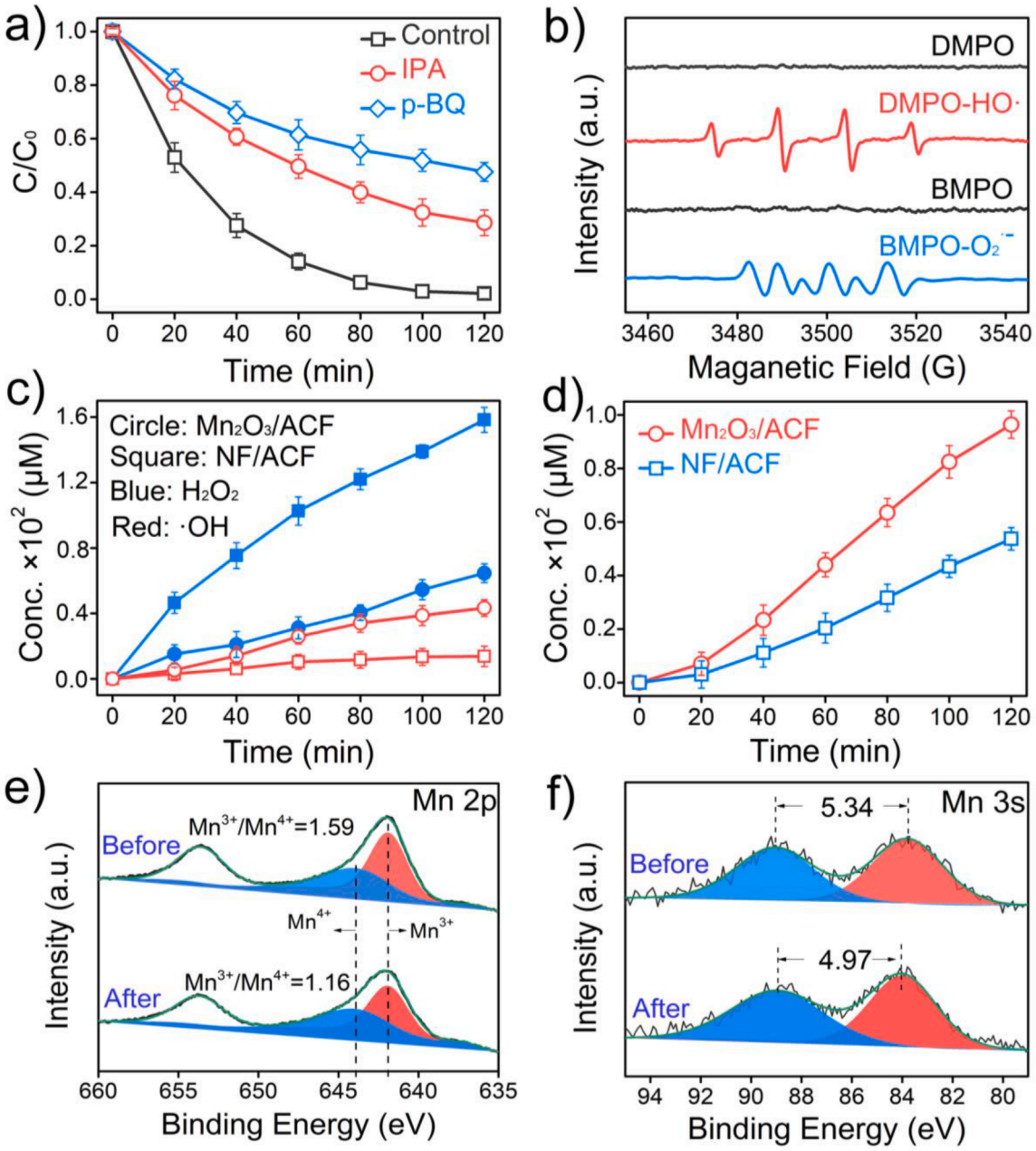

Fig. 2. (a) Removal efficiency of cyanides with the addition of different scavengers; (b) EPR spectra obtained with the addition of DMPO or BMPO in the EF process. (c) Variation of H_2O_2 and $^{\bullet}OH$ concentrations in the Mn_2O_3/ACF and NF/ACF systems; (d) Variation of $^{\bullet}O_2^-$ concentrations in the Mn_2O_3/ACF and NF/ACF systems; XPS spectra of Mn2p (e) and Mn3s (f) of Mn_2O_3 anode before and after the reaction. Reaction conditions: [CN^-] = 1.35 mM, [IPA] = [p-BQ] = 20 mM, [DMPO] = [BMPO] = 100 mM, [Na_2SO_4] = 100 mM, bias potential = 2.5 V, initial pH = 11.50, T = 298 K.

electrode increased from 15.4 to 58.5% (w/w). As a consequence, the removal efficiency of CN^- in the EF system increased from 86.1 to 98.2%. Previous reports revealed that the efficiency of H_2O_2 activation and pollutants removal were closely related to the content of manganese (Eq. (12)) (He et al., 2019; Ge et al., 2021). However, when the manganese source dosage continued to increase to 4 mM, the CN^- removal performance remained stable. It is known that the metal vacancies etched by HCl on the nickel foam were certain, which resulted in the manganese content on the bulk electrode could have a saturation value. The saturated manganese content on the bulk electrode was analyzed at around 60% (w/w) (detailed analysis is shown in Table S1). Therefore, when the manganese source was 3 mM or 4 mM, the manganese content on the bulk electrode reached saturation. Moreover, as shown in Fig. S6c, d and Table S2, the removal efficiency of CN^- increased from 58.4 to 98.2% with the increase in bias potential from 1.0 V to 2.5 V. Nevertheless, when the bias voltage continued to increase to 3.0 V, the removal performance of CN^- will not be enhanced. Through the linear sweep voltammetry curves of Mn_2O_3 anode and ACF cathode (Fig. S7), it can be found that the oxygen evolution reaction potential of Mn_2O_3 anode and hydrogen evolution reaction potential of ACF cathode was 1.52 V (vs. Ag/AgCl) and -2.21 V (vs. Ag/AgCl), respectively. As a result, excessive bias potential could cause severe secondary reactions between the cathode and anode (hydrogen evolution and oxygen evolution). Based on the above results, all subsequent removal experiments were conducted with a 3 mM of manganese source in anode preparation and a bias voltage of 2.5 V.

$$\equiv Mn(III)/Mn(III) + H_2O_2 \rightarrow \equiv Mn(IV)/Mn(IV) + {}^{\bullet}OH + OH^- \quad (12)$$

In addition, different anodes and cathodes were substituted in the CN^- removal process to investigate the synergistic effect between Mn_2O_3 and ACF in the EF system. As shown in Fig. S8 in the SI, when Mn_2O_3 and ACF were used as anode and cathode, respectively, 98.2% of CN^- was removed within 120 min. Besides, in the nickel foam (NF)/ACF, NF/platinum, and Mn_2O_3/platinum systems, the removal efficiency of CN^- was 42.7%, 70.8% and 94.1%, respectively, which are all much lower than that in the EF system. Furthermore, when dissolved oxygen (O_2) in the EF system was evicted by Ar gas, only 50% of CN^- was removed in 120 min (Fig. S9 in the SI). In conclusion, these results indicate that there is a noticeable synergistic effect between Mn_2O_3 and ACF in the EF system, favoring the formation of active species by activating the dissolved O_2 to achieve efficient CN^- removal.

To further explore the mineralization performance of CN^- in the EF system, the concentration variation of different nitrogen species during the catalytic process was identified under the optimal reaction conditions. As shown in Fig. 1b, the TN concentration remained stable for 120 min, indicating that almost no gaseous nitrogen or HCN was generated. Besides, some CNO^-, which originated from excessive ultraviolet radiation in the photolysis process, existed only before the EF reaction and could be promptly converted into NH_4^+/NH_3 with the ongoing EF reaction. 0.14 mM of NH_4^+/NH_3 was generated during the EF process and its concentration was nearly close to that of the initial CNO^-. Moreover, no CNO^- was detected during the CN^- removal process. The main conversion product of CN^- in the EF system was NO_3^-, which was different from previous reports that CNO^- was the dominant oxidation intermediate in AOPs (Zhao et al., 2015; Chen et al., 2014; Qi et al., 2017; Qiao et al., 2020). The concentration of NO_3^- increased gradually with the decrease of CN^- within 120 min. Hence, the mineralization efficiency of CN^- was calculated to be 92.9% after 120 min. In addition, to further illustrate the advantage of the proposed EF system, the removal and mineralization performance of CN^- in two previously reported EF systems were compared (Zhang et al., 2022; Dung et al., 2021). As shown in Fig. S10, the removal and mineralization performance of CN^- in the previously reported EF systems were far below that in the EF system proposed in this study, indicating that the EF system (Mn_2O_3 as anode and ACF as cathode) had excellent performance in CN^- removal and mineralization.

To evaluate the practical application of EF system, five cycling tests were carried out to investigate its stability (Hodges et al., 2018). As shown in Fig. S11 in the SI, the EF system showed outstanding removal and mineralization performance of cyanides in each cycle and a negligible decrease was observed in the final cycle. Besides, we determined the dissolution concentration of manganese ion after each cycle and the dissolution concentration of manganese was all less than 0.1 ppm after each cycle (Fig. S12 in the SI). Moreover, the SEM image and XRD pattern of Mn_2O_3 after 5 cycles revealed that no obvious changes were observed in the morphology and structure compared to that of the primary sample (Figs. S13 and S14 in the SI). These results indicate that the EF system has good stability. In addition, the energy consumption (EC) of EF system was calculated as 167 kWh/m^3, which is lower than the EC in the other two reported EF systems and in the previous literature (Table S3) (Mudliar et al., 2009; Castilla-Acevedo et al., 2020). In conclusion, this EF system has excellent application potential in the treatment of cyanide-containing wastewater.

3.3. Determination of active species

To determinate active species involved in the removal process of CN^-, active species quenching experiments were carried out. Isopropanol (IPA) and p-benzoquinone (p-BQ) were chosen as scavengers for $^\bullet OH$ ($k^\bullet OH/IPA = 1.9 \times 10^9\ M^{-1}s^{-1}$) and $^\bullet O_2^-$ ($k^\bullet O_2^-/BQ = 1.0 \times 10^9\ M^{-1}s^{-1}$), respectively (Ye et al., 2020; Zhang et al., 2021). As shown in Fig. 2a, when excess IPA and p-BQ were added to the EF system, respectively, the removal efficiency of cyanides was distinctly limited and only 71% and 52% of CN^- were removed within 120 min, respectively. Given that the generation of $^\bullet OH$ is derived from $^\bullet O_2^-$, the inhibitory effect of p-BQ was more severe than that of IPA. Besides, furfuryl alcohol (FFA), pyrophosphate (PP) and NO_3^- were chosen as the scavengers for $^1O_2$ ($k^1O_2/FFA = 1.0 \times 10^8\ M^{-1}s^{-1}$), dissolved manganese species and hydrated electron (e_{aq}^-) ($ke_{aq}^-/NO_3^- = 9.7 \times 10^9\ M^{-1}s^{-1}$), respectively (Yin et al., 2018; Liu et al., 2019; Xiao et al., 2017). As shown in Fig. S15 in the SI, the addition of FFA, PP and NO_3^- did not inhibit the removal of CN^-. Moreover, it can be found that there were no obvious oxidation peaks in the cyclic voltammetry (CV) curves in the EF system in presence of CN^- (Fig. S16). These results indicated $^1O_2$, dissolved manganese species and direct electrooxidation did not contribute to CN^- removal. Furthermore, methyl alcohol (MeOH) and p-hydroxybenzonic acid (p-HBA) were used as the scavenger and the probe for $SO_4^{\bullet-}$, respectively (Zou et al., 2018; Oh et al., 2017). As shown in Fig. S17, the inhibition of MeOH was closed to that of IPA and there was no obvious peak of specific p-benzoquinone (p-BQ) observed in the high-performance liquid chromatogram of p-HBA probe, indicating $SO_4^{\bullet-}$ was not generated and did not contribute to the cyanides removal in the EF system. In conclusion, $^\bullet O_2^-$ and $^\bullet OH$ were successfully generated in the EF system and played a vital role in the cyanides removal process. Moreover, EPR was used to further verify the presence of $^\bullet OH$ and $^\bullet O_2^-$ in the EF system. As shown in Fig. 2b, no EPR signals were detected with DMPO or BMPO alone. As the reaction progressed, the signals for additive $^\bullet OH$ and $^\bullet O_2^-$ adducts were detected (Qiao et al., 2020), demonstrating that $^\bullet OH$ and $^\bullet O_2^-$ were formed in the EF system.

3.4. Production mechanism of active species

To further explore the mechanism of active oxygen species (ROS) production, the concentrations of H_2O_2, $^\bullet OH$ and $^\bullet O_2^-$ in the different systems were monitored. As shown in Fig. 2c, d, when pristine NF was used as the anode, the concentrations of H_2O_2, $^\bullet OH$ and $^\bullet O_2^-$ were 158.1, 13.7, and 53.7 μM, respectively, after 120 min in the absence of cyanides. Whereas, when Mn_2O_3 was used as the anode, the concentrations of H_2O_2, $^\bullet OH$ and $^\bullet O_2^-$ were 64.6, 43.3, and 96.4 μM, respectively. Compared with the pristine NF anode, the concentration of H_2O_2 decreased but the concentrations of $^\bullet OH$ and $^\bullet O_2^-$ increased drastically when Mn_2O_3 was used, confirming that H_2O_2 can be effectively activated by the Mn_2O_3 anode. Furthermore, as shown in Fig. S18 in the SI, once the dissolved O_2 in the solution was completely evicted by Ar gas, almost no H_2O_2 and free radicals ($^\bullet OH$ and $^\bullet O_2^-$) were generated in the EF system, indicating that the ROS originated from the activation of dissolved O_2 by the ACF cathode and not from the oxidation of H_2O by the Mn_2O_3 anode Eqs. (7)–((9)).

$$AOS = 8.956 - 1.126 \times \Delta E_S \quad (13)$$

Moreover, XPS was used to further analyze the effect of the Mn_2O_3 anode on ROS generation. The Mn $2p_{3/2}$ XPS spectra are shown in Fig. 2e, and the peaks around 642.3 and 644.3 eV were assigned to Mn^{3+} and Mn^{4+}, respectively (Li et al., 2018). After 120 min of EF reaction, the Mn^{3+}/Mn^{4+} content ratio decreased from 1.59 to 1.16. In addition, the average oxidation states (AOS) of Mn before and after the reaction were estimated based on the Eq. (13), where ΔE_s is the splitting energy of Mn 3s peaks (Yang et al., 2020). As shown in Fig. 2f, the AOS increased from 2.94 to 3.36 after EF reaction, confirming the existence of higher valence Mn species, i.e., Mn^{4+}. The XPS results further verify that the EF process involved the transformation of Mn^{3+}/Mn^{4+}, which played a vital role in the activation of H_2O_2 to form ROS (Eq. (10)). In summary, there was a prominent synergistic effect between the Mn_2O_3 anode and ACF cathode in the EF system to effectively produce $^\bullet OH$ and $^\bullet O_2^-$, which has greatly accelerated the cyanide mineralization performance.

3.5. Mineralization mechanism of cyanides

In the EF system, 92.9% of CN^- could be transformed into NO_3^-

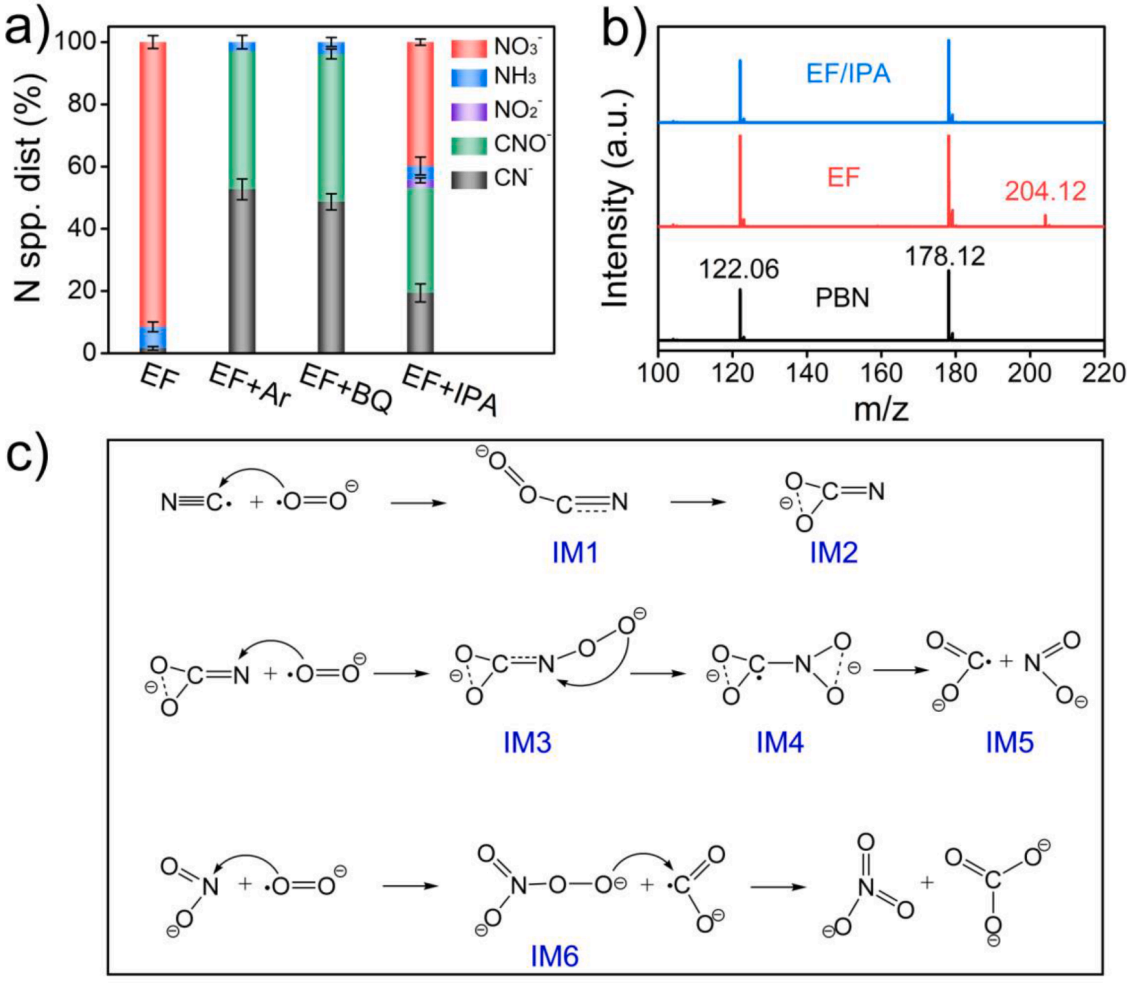

Fig. 3. (a) Oxidation products of cyanide in the different systems; (b) Mass spectrum of PBN during the cyanide mineralization process in the EF and EF/IPA system; (c) Possible pathways for the transformation of $^{\bullet}CN$ to NO_3^- with $^{\bullet}O_2^-$. Reaction conditions: $[CN^-] = 1.35$ mM, [IPA] = [BQ] = 20 mM, [PBN] = 10 mM, $[Na_2SO_4] = 100$ mM, bias potential = 2.5 V, initial pH = 11.50, T = 298 K.

within 120 min Fig. 1b), different from the previous reports that the transformation products of CN^- in the AOPs were only CNO^- (Table S4). In order to explore whether the formation of NO_3^- derived from the subsequent conversion of CNO^- intermediates (Eqs. (1)–((3)), we selected potassium cyanate (KCNO) as the pollutant in place of CN^- in the EF system. Since the conversion of CNO^- is critically dependent on the alkalinity of the system Koo et al., 2021), the variation of the pH value during the EF process was monitored firstly. As shown in Fig. S19 in the SI, the initial pH value of the ferricyanide solution was adjusted to 12.00. After photolysis, the pH value dropped to 11.50, lower than the p*K*a of H_2O_2/HO_2^- (11.62) (Cochemé et al., 2012). After 120 min of EF reaction, the pH value declined to 9.82. Subsequently, the oxidation products of CNO^- in the EF system with different initial concentrations (10 ppm and 30 ppm) were investigated at pH values of 9.82 and 11.50, respectively. As shown in Table S5 in the SI, although CNO^- could hydrolyze in the EF system, the formations of NO_3^- were all less than 0.3% after 120 min of reaction under different initial concentrations and pH values, demonstrating that CNO^- could not be converted to NO_3^- in the EF system. Therefore, it can be concluded that the fast conversion between CN^- and NO_3^- in the EF system did not occur via CNO^- intermediate, which is different from the traditional mineralization path of CN^- (Eqs. (1)–((3)). Hence, a new mechanism should be proposed to explain the transformation of CN^- into NO_3^- in the EF system.

To study the effect of $^{\bullet}OH$ and $^{\bullet}O_2^-$ on the mineralization of CN^-, excess Ar gas, p-BQ or IPA were added to the EF system, respectively. As shown in Fig. 3 and Table S6, under continuous bubbling of Ar gas, CN^- was converted to CNO^- (93.8%) and NH_3/NH_4^+ (6.2%) in the EF system, indicating that the conversion between CN^- and NO_3^- could not be realized in the absence of ROS. In this case, CN^- was electrostatically attracted to the anode surface and was oxidized to CNO^- through direct electron transfer, which could be observed from the CV curve of the EF/Ar system with CN^- (Fig. S20 in the SI). Besides, the same phenomenon could be observed after adding excess p-BQ. CN^- was converted to CNO^- (90.9%) and NH_3/NH_4^+ (9.1%) with no NO_3^- generating. Because the active species was derived from the further conversion of $^{\bullet}O_2^-$, CN^- could only be oxidized through direct electron transfer once $^{\bullet}O_2^-$ was quenched. Furthermore, after the addition of excess IPA in the EF system, only $^{\bullet}O_2^-$ could exist and the oxidation products of CN^- were CNO^- (41.9%), NO_3^- (49.4%), NO_2^- (3.0%), and NH_3/NH_4^+ (5.7%), which reveals that $^{\bullet}O_2^-$ played a decisive role in the conversion between CN^- and NO_3^-. Moreover, without adding p-BQ, IPA and Ar gas, both $^{\bullet}OH$ and $^{\bullet}O_2^-$ existed and CN^- could be more effectively transformed into NO_3^- (92.9%) and NH_3/NH_4^+ (7.1%) in the EF system, much superior to the system only containing $^{\bullet}O_2^-$. As reported that CN^- could be preferentially activated into $^{\bullet}CN$ by $^{\bullet}OH$ (Zhao et al., 2015), N-tert-butyl-α-phenylnitrone (PBN) was added to the EF system to capture the possible formed $^{\bullet}CN$, and the addition-products were detected through the Mass spectrum (Qin et al., 2020). As shown in Figs. 3b and S21, before the reaction, the m/z 178.12 (M+1) and 122.06 (M+1) were attributed to the raw PBN and the benzaldehyde oxime (the

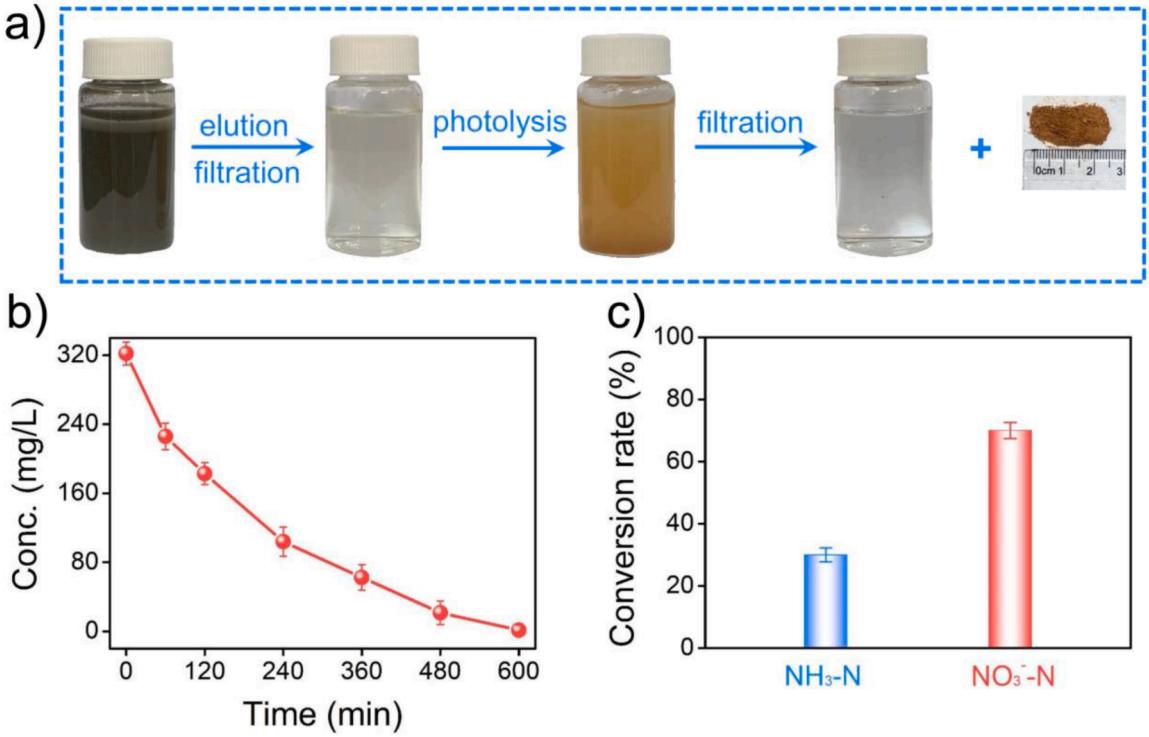

Fig. 4. (a) Schematic diagram of actual cyanide residue pretreatment; (b) Cyanide removal performance in the EF system; (c) Distribution of the products after the EF reaction for 10 h.

decomposition product of PBN), respectively (Imaram et al., 2010). With the EF reaction progress, a low peak at 204.12 (M+1) was present and it was assigned to the PBN-CN adducts, indicating that $^{\bullet}CN$ can be generated in the EF system. However, when excess IPA was added, the peak of PBN-CN adducts was not detected, confirming that CN^- could not be activated into $^{\bullet}CN$ by $^{\bullet}O_2^-$ or electron. Compared with CN^-, $^{\bullet}CN$ is in an electron-deficient state and has higher activity, resulting in that it is more inclined to react with electron-donor $^{\bullet}O_2^-$ to impede its self-quenching, avoiding the formation of CNO^- and facilitating the efficient mineralization of CN^-. Therefore, there was a prominent synergistic effect between $^{\bullet}OH$ and $^{\bullet}O_2^-$ in the EF system, which subverted the traditional mineralization path of CN^-.

Density functional theory (DFT) calculations were further introduced to better understand the mechanism of cyanide mineralization synergistically mediated by $^{\bullet}O_2^-$ and $^{\bullet}OH$. Details of the calculations are present in Text S4 in the SI. Full geometry optimizations in the aqueous solution were performed to locate all the stationary points, using the M062X method with the def2tzvpp basis set for all atoms and all geometry calculations were performed with the Gaussian 09 program. Due to the difference in redox potential, $^{\bullet}OH$ is the strong electron acceptor, while $^{\bullet}O_2^-$ is the electron donor. Therefore, free cyanides can be preferentially activated into electron-deficient $^{\bullet}CN$ by $^{\bullet}OH$ through electron transfer (consistent with Fig. 3b), without transition state (TS) or energy barrier. Subsequently, $^{\bullet}O_2^-$ reacts with the generated $^{\bullet}CN$ via nucleophilic addition to prevent the self-quenching of $^{\bullet}CN$. The detailed reaction pathway of $^{\bullet}CN$ and $^{\bullet}O_2^-$ is shown in Fig. 3c and the transition states are listed in Table S7. Firstly, $^{\bullet}O_2^-$ preferentially nucleophilically attacked the carbon on the $^{\bullet}CN$ to form intermediate 1 (IM1). Therein, the oxygen in IM1, which was not involved in the bonding, dissociates and then nucleophilically attacked the C atom to form a C-O bond (IM2). Secondly, another $^{\bullet}O_2^-$ was introduced and attacked the nitrogen of IM2 to form IM3. The other oxygen in IM3, which was not involved in the bonding, would then nucleophilically attack the nitrogen to form an N-O bond (IM4). Due to the difference in electronegativity of carbon, nitrogen and oxygen, the carbon atom would be in an electron-deficient state and an electron would be released during the formation of the N-O bond. The C-N bond in IM4 was cleaved to produce NO_2^- and $^{\bullet}CO_2^-$ (IM5). Thirdly, $^{\bullet}O_2^-$ was introduced and attacked the nitrogen of NO_2^- to form IM6. The other oxygen in IM6, which was not involved in the bonding, then nucleophilically attacked the $^{\bullet}CO_2^-$ and the O-O bond on TS7 was broken, eventually forming NO_3^- and CO_3^{2-}. 0.032 mM of NO_2^- were detected in the EF/IPA system, whereas in EF systems, NO_2^- was quickly converted into NO_3^- (Fig. 3a), resulting from the presence of more $^{\bullet}O_2^-$ (Fig. S22 in the SI). As shown in Fig. S23, the energy profiles of the nucleophilic addition reveal that the conversion between IM3 and IM4 is the rate-limiting step of the entire nucleophilic addition process, and the activation energy required for the reaction of $^{\bullet}O_2^-$ and $^{\bullet}CN$ is 46.0 kcal mol^{-1}, suggesting that the nucleophilic addition of $^{\bullet}CN$ with $^{\bullet}O_2^-$ is energetically feasible.

In summary, the mineralization mechanism of CN^- in the EF system is summarized as follows: CN^- first reacts with $^{\bullet}OH$ to generate $^{\bullet}CN$ (Eq. (4)). Subsequently, $^{\bullet}CN$ undergoes nucleophilic addition with $^{\bullet}O_2^-$ to be rapidly converted to NO_3^- (Eq. (14)), avoiding the self-quenching of $^{\bullet}CN$ and achieving the efficient mineralization of CN^-.

$$^{\bullet}CN + 3^{\bullet}O_2^- \rightarrow NO_3^- + CO_3^{2-} \quad (14)$$

3.6. *Treatment of actual ferricyanide eluent*

To confirm the practical application of this novel EF system, the actual eluent of the cyanide residue was used as the treatment object. The composition of the cyanide residue provided by the Zhaojin Group (Shandong, China) is shown in Table S8 in the SI. Besides, the elution method of cyanide residue is presented in Text S5 in the SI and the eluent with ferricyanide was obtained. The composition of the eluent is shown in Table S9. Firstly, the eluent was treated by photolysis. As shown in Fig. 4a, the 106 mg iron sludge could be recycled and the free cyanide concentration increased from 33.4 to 321.9 mg/L after photolysis. Moreover, the concentration of free cyanide was similar to that of total

cyanide, indicating that all metal-cyanide complexes were converted to free cyanide. The solution of free cyanide was transferred to the EF system. As shown in Fig. 4b, about 99.4% of CN^- was removed after 10 h of EF reaction. The oxidation products of CN^- were detected and about 70.02% of CN^- was converted to NO_3^- and 29.98% of CN^- was transformed to NH_3 after subtracting the initial concentration of NO_3^- and NH_3 (Fig. 4c). And NH_3 was derived from CNO^- that was formed mainly due to excessive UV radiation in the photolysis process, which could be avoided by optimizing the UV irradiation time. In conclusion, the EF system combined with UV photolysis pretreatment was able to effectively achieve mineralization of the actual ferricyanide eluent, indicating that the EF system has good potential for treating actual cyanide-containing effluents.

4. Conclusion

In the traditional methods of CN^- mineralization, the inhibition of HCN evolution and the efficient hydrolysis of CNO^- intermediate cannot be simultaneously achieved, where CNO^- with toxicity was the only conversion product of CN^- but not NO_3^-. In this study, we developed a novel Electro-Fenton system to simultaneously generate $^{\bullet}OH$ and $^{\bullet}O_2^-$, realizing efficient mineralization of CN^- released by the photolysis of ferricyanide. In contrast to the traditional CN^- conversion pathway, a new mineralization mechanism has been proposed in the EF system. Noteworthily, CN^- was activated into electron-deficient $^{\bullet}CN$ by $^{\bullet}OH$ preferentially, and then the $^{\bullet}CN$ intermediate reacted with $^{\bullet}O_2^-$ via nucleophilic addition to rapidly form NO_3^- in the novel EF system. Besides, the entire reaction process was carried out under strongly alkaline conditions, effectively preventing the formation of highly toxic HCN. Moreover, this strategy shows the feasibility of the practical application, which can realize the effective mineralization of the actual cyanide residue eluent. The present work develops a novel pathway of CN^- mineralization to form NO_3^- but not CNO^- and opens a new avenue to invent good technologies for highly efficient treatment of effluents contaminated with cyanides and cyanocomplexes.

Declaration of Competing Interest

The authors declare that they have no known competing financial interests or personal relationships that could have appeared to influence the work reported in this paper.

Acknowledgments

We gratefully acknowledge the financial support of the National Natural Science Foundation of China (52170082, 51878325, 51868050, and 51938007) and the National Key R&D Program of China (2018YFC1902002). We would like to express our gratitude to EditSprings (https://www.editsprings.com) for the expert linguistic services provided.

Supplementary materials

Supplementary material associated with this article can be found, in the online version, at doi:10.1016/j.watres.2021.117890.

References

Akcil, A., 2003. Destruction of cyanide in gold mill effluents: biological versus chemical treatments. Biotechnol. Adv. 21 (6), 501–511. https://doi.org/10.1016/S0734-9750(03)00099-5.

APHA, AWWA, WEF, 2012. Standard Methods for the Examination of Water and Wastewater, 22th Ed. APHA, Washington, DC.

Castilla-Acevedo, S.F., Betancourt-Buitrago, L.A., Dionysiou, D.D., Machuca-Martínez, F., 2020. Ultraviolet light-mediated activation of persulfate for the degradation of cobalt cyanocomplexes. J. Hazard. Mater. 392, 122389 https://doi.org/10.1016/j.jhazmat.2020.122389.

Chen, F.Y., Zhao, X., Liu, H.J., Qu, J.H., 2014. Reaction of $Cu(CN)_3^{2-}$ with H_2O_2 in water under alkaline conditions: cyanide oxidation, Cu^+/Cu^{2+} catalysis and H_2O_2 decomposition. Appl. Catal. B Environ. 158-159, 85–90. https://doi.org/10.1016/j.apcatb.2014.04.010.

Chen, Y., Zhang, X., Feng, S.X., 2018. Contribution of the excited triplet state of humic acid and superoxide radical anion to generation and elimination of phenoxyl radical. Environ. Sci. Technol. 52 (15), 8283–8291. https://doi.org/10.1021/acs.est.8b00890.

Cochemé, H.M., Logan, A., Prime, T.A., Abakumova, I., Quin, C., McQuaker, S.J., Patel, J. V., Fearnley, A.M., James, A.M., Porteous, C.M., Smith, R.A.J., Hartley, R.C., Partridge, L., Murphy, M.P., 2012. Using the mitochondria-targeted ratiometric mass spectrometry probe MitoB to measure H_2O_2 in living drosophila. Nat. Protoc. 7, 946–958. https://doi.org/10.1038/nprot.2012.035.

Dash, R.R., Gaur, A., Balomajumder, C., 2009a. Cyanide in industrial wastewaters and its removal: a review on biotreatment. J. Hazard. Mater. 163 (1), 1–11. https://doi.org/10.1016/j.jhazmat.2008.06.051.

Dash, R.R., Balomajumder, C., Kumar, A., 2009b. Removal of cyanide from water and wastewater using granular activated carbon. Chem. Eng. J. 146 (3), 408–413. https://doi.org/10.1016/j.cej.2008.06.021.

Ding, X., Zhao, K., Zhang, L.Z., 2014. Enhanced photocatalytic removal of sodium pentachlorophenate with self-doped Bi_2WO_6 under visible light by generating more superoxide ions. Environ. Sci. Technol. 48 (10), 5823–5831. https://doi.org/10.1021/es405714q.

Dung, N.T., Duong, L.T., Hoa, N.T., Thao, V.D., Ngan, L.V., Huy, N.N., 2021. A comprehensive study on the heterogeneous Electro-Fenton degradation of tartrazine in water using $CoFe_2O_4$/carbon felt cathode. Chemosphere 287, 132141. https://doi.org/10.1016/j.chemosphere.2021.132141.

Ge, L.F., Yue, Y.M., Wang, W., Tan, F.T., Zhang, S.H., Wang, X.Y., Qiao, X.L., Wong, P.K., 2021. Efficient degradation of tetracycline in wide pH range using MgNCN/MgO nanocomposites as novel H_2O_2 activator. Water Res. 198, 117149 https://doi.org/10.1016/j.watres.2021.117149.

Grieken, R., Aguado, J., López-Muñoz, M., Marugán, J., 2005. Photocatalytic degradation of iron-cyanocomplexes by TiO_2 based catalysts. Appl. Catal. B Environ. 55 (3), 201–211. https://doi.org/10.1016/j.apcatb.2004.08.008.

He, D.W., Niu, H.Y., He, S.J., Mao, L., Cai, Y.Q., Liang, Y., 2019. Strengthened Fenton degradation of phenol catalyzed by core/shell Fe-Pd@C nanocomposites derived from mechanochemically synthesized Fe-metal organic frameworks. Water Res. 162, 151–160. https://doi.org/10.1016/j.watres.2019.06.058.

He, X., Sun, B., He, M.R., Chi, H.Z., Wang, Z., Zhang, W., Ma, J., 2020. Highly efficient simultaneous catalytic degradation and defluorination of perfluorooctanoic acid by the H_2O_2-carbon/MnO_2 system generating $O_2^{\bullet-}$ and•OH synchronously. Appl. Catal. B Environ. 277, 119219 https://doi.org/10.1016/j.apcatb.2020.119219.

Hodges, B.C., Cates, E.L., Kim, J.H., 2018. Challenges and prospects of advanced oxidation water treatment processes using catalytic nanomaterials. Nat. Nanotechnol. 13, 642–650. https://doi.org/10.1038/s41565-018-0216-x.

Imaram, W., Gersch, C., Kim, K.M., Johnson, R.J., Henderson, G.N., Angerhofer, A., 2010. Radicals in the reaction between peroxynitrite and uric acid identified by electron spin resonance spectroscopy and liquid chromatography mass spectrometry. Free Radic. Biol. Med. 49 (2), 275–281. https://doi.org/10.1016/j.freeradbiomed.2010.04.010.

Joo, S.H., Feitz, A.J., Sedlak, D.L., Waite, T.D., 2005. Quantification of the oxidizing capacity of nanoparticulate zero-valent iron. Environ. Sci. Technol. 39 (5), 1263–1268. https://doi.org/10.1021/es048983d.

Johnson, C., 2015. The fate of cyanide in leach wastes at gold mines: an environmental perspective. Appl. Geochem. 57, 194–205. https://doi.org/10.1016/j.apgeochem.2014.05.023.

Koo, M.S., Kim, H., Lee, K.E., Choi, W., 2021. Photoconversion of cyanide to dinitrogen using the durable electrode of a TaON overlayer-deposited WO_3 film and visible light. ACS EST Eng. 1 (2), 228–238. https://doi.org/10.1021/acsestengg.0c00070.

Kuyucak, N., Akcil, A., 2013. Cyanide and removal options from effluents in gold mining and metallurgical processes. Mineral Eng. 50-51, 13–29. https://doi.org/10.1016/j.mineng.2013.05.027.

Li, Q., Huang, X., Su, G., Zheng, M., Huang, C., Wang, M., Ma, C., Wei, D., 2018. The regular/persistent free radicals and associated reaction mechanism for the degradation of 1,2,4-trichlorobenzene over different MnO_2 polymorphs. Environ. Sci. Technol. 52 (22), 13351–13360. https://doi.org/10.1021/acs.est.8b03789.

Liu, W.F., Sun, B., Qiao, J.L., Guan, X.H., 2019. Influence of pyrophosphate on the generation of soluble Mn(III) from reactions involving Mn oxides and Mn(VII). Environ. Sci. Technol. 53, 10227–10235. https://doi.org/10.1021/acs.est.9b03456.

Lu, Z.Y., Chen, G.X., Siahrostami, S., Chen, Z.H., Liu, K., Xie, J., Liao, L., Wu, T., Lin, D.C., Liu, Y.J., Jaramillo, T.F., Nørskov, J.K., Cui, Y., 2018. High-efficiency oxygen reduction to hydrogen peroxide catalyzed by oxidized carbon materials. Nat. Catal. 1, 156–162. https://doi.org/10.1038/s41929-017-0017-x.

Luo, Z.H., Tseng, M.Y., Minakata, D., Bai, L., Hu, W.P., Song, W.H., Wei, Z.S., Spinney, R., Dionysiou, D.D., Xiao, R.Y., 2021. Mechanistic insight into superoxide radical-mediated degradation of carbon tetrachloride in aqueous solution: an *in situ* spectroscopic and computational study. Chem. Eng. J. 410, 128181 https://doi.org/10.1016/j.cej.2020.128181.

Ma, J.Z., Nie, J.X., Zhou, H.X., Wang, H., Lian, L.S., Yan, S.W., Song, W.H., 2020. Kinetic consideration of photochemical formation and decay of superoxide radical in dissolved organic matter solutions. Environ. Sci. Technol. 54 (6), 3199–3208. https://doi.org/10.1021/acs.est.9b06018.

McDowell, M.S., Bakac, A., Espenson, J.H., 1983. A convenient route to superoxide ion in aqueous solution. Inorg. Chem. 22 (5), 847–848. https://doi.org/10.1021/ic00147a033.

Mitchell, S.M., Ahmad, M., Teel, A.L., Watts, R.J., 2013. Degradation of perfluorooctanoic acid by reactive species generated through catalyzed H_2O_2 propagation reactions. Environ. Sci. Technol. Lett. 1 (1), 117–121. https://doi.org/10.1021/ez4000862.

Mudliar, R., Umare, S.S., Ramteke, D.S., Wate, S.R., 2009. Energy efficient—advanced oxidation process for treatment of cyanidecontaining automobile industry wastewater. J. Hazard. Mater. 164, 1474–1479. https://doi.org/10.1016/j.jhazmat.2008.09.118.

Novak, D., Franke-Whittle, I.H., Pirc, E.T., Jerman, V., Insam, H., Logar, R.M., Stres, B., 2013. Biotic and abiotic processes contribute to successful anaerobic degradation of cyanide by UASB reactor biomass treating brewery waste water. Water Res. 47 (11), 3644–3653. https://doi.org/10.1016/j.watres.2013.04.027.

Oh, W.D., Dong, Z.L., Ronn, G., Lim, T.T., 2017. Surface-active bismuth ferrite as superior peroxymonosulfate activator for aqueous sulfamethoxazole removal: Performance, mechanism and quantification of sulfate radical. J. Hazard. Mater. 325, 71–81. https://doi.org/10.1016/j.jhazmat.2016.11.056, 2017.

Qi, F.J., Yang, B., Wang, Y.B., Mao, R., Zhao, X., 2017. H_2O_2 assisted photoelectrocatalytic oxidation of Ag-cyanide complexes at metal-free gC_3N_4 photoanode with simultaneous Ag recovery. ACS Sustain. Chem. Eng. 5 (6), 5001–5006. https://doi.org/10.1021/acssuschemeng.7b00395.

Qiao, M., Wu, X.F., Zhao, S., Djellabi, R., Zhao, X., 2020. Peroxymonosulfate enhanced photocatalytic decomposition of silvercyanide complexes using g-C_3N_4 nanosheets with simultaneous recovery of silver. Appl. Catal. B Environ. 265, 118587 https://doi.org/10.1016/j.apcatb.2020.118587.

Qin, L., Huang, C.H., Mao, L., Shao, B., Zhu, B.Z., 2020. First unequivocal identification of the critical acyl radicals from the antituberculosis drug isoniazid and its hydrazide analogs by complementaryapplications of ESR spin-trapping and HPLC/MS methods. Free Radic. Biol. Med. 154, 1–8. https://doi.org/10.1016/j.freeradbiomed.2020.04.021.

Teo, W.K., Tan, T.C., 1987. Hypochlorite oxidation of cyanate under mildly alkaline conditions. Water Res. 21 (6), 677–682. https://doi.org/10.1016/0043-1354(87)90078-9.

Tian, N., Tian, X.K., Nie, Y.L., Yang, C., Zhou, Z.X., Li, Y., 2019. Enhanced 2, 4-dichlorophenol degradation at pH 3-11 by peroxymonosulfate via controlling the reactive oxygen species over Ce substituted 3D Mn_2O_3. Chem. Eng. J. 355, 448–456. https://doi.org/10.1016/j.cej.2018.08.183.

Xiao, Q., Wang, T., Yu, S.L., Yi, P., Li, L., 2017. Influence of UV lamp, sulfur (IV) concentration, and pH on bromate degradation in UV/sulfite systems: mechanisms and applications. Water Res. 111, 288–296. https://doi.org/10.1016/j.watres.2017.01.018.

Xiao, K., Zhou, B., Chen, S.Y., Yang, B., Zhang, J.M., Zhu, C.Z., 2019. Enhanced photoelectrocatalytic breakdown of Cu-cyanide complexes and copper recovery using photoelectrogenerated free chlorine. Electrochem. Commun. 100, 34–38. https://doi.org/10.1016/j.elecom.2019.01.018.

Yang, W.H., Peng, Y., Wang, Y., Wang, Y., Liu, H., Su, Z.A., Yang, W.N., Chen, J.J., Si, W. Z., Li, J.H., 2020. Controllable redox-induced *in-situ* growth of MnO_2 over Mn_2O_3 for toluene oxidation: active heterostructure interfaces. Appl. Catal. B Environ. 278, 119279 https://doi.org/10.1016/j.apcatb.2020.119279.

Ye, Z.H., Brillas, E., Centellas, F., Cabot, P.L., Sirés, I., 2020. Expanding the application of photo Electro-Fenton treatment to urban wastewater using the Fe(III)-EDDS complex. Water Res. 169, 115219 https://doi.org/10.1016/j.watres.2019.115219.

Yin, R.L., Guo, W.Q., Wang, H.Z., Du, J.S., Zhou, X.J., Wu, Q.L., Zheng, H.S., Chang, J.S., Ren, N.Q., 2018. Selective degradation of sulfonamide antibiotics by peroxymonosulfate alone: direct oxidation and nonradical mechanisms. Chem. Eng. J. 334, 2539–2546. https://doi.org/10.1016/j.cej.2017.11.174.

Zhang, D.Y., Liu, T.C., Yin, K., Liu, C.B., Wei, Y.F., 2020. Selective H_2O_2 production on N-doped porous carbon from direct carbonization of metal organic frameworks for Electro-Fenton mineralization of antibiotics. Chem. Eng. J. 383, 123184 https://doi.org/10.1016/j.cej.2019.123184.

Zhang, L.S., Jiang, X.H., Zhong, Z.A., Tian, L., Sun, Q., Cui, Y.T., Lu, X., Zou, J.P., Luo, S. L., 2021. Carbon nitride supported high-loading Fe single-atom catalyst for activating of peroxymonosulfate to generate $^1O_2$ with 100% selectivity. Angew. Chem. Int. Ed. 133, 1–6. https://doi.org/10.1002/anie.202109488.

Zhang, J.J., Qiu, S., Feng, H.P., Hu, T., Wu, Y.X., Luo, T., Tang, W.W., Wang, D.B., 2022. Efficient degradation of tetracycline using core–shell Fe@Fe_2O_3-CeO_2 composite as novel heterogeneous Electro-Fenton catalyst. Chem. Eng. J. 428, 131403 https://doi.org/10.1016/j.cej.2021.131403.

Zhao, H., Qian, L., Guan, X.H., Wu, D.L., Zhao, G.H., 2016. Continuous bulk FeCuC aerogel with ultradispersed metal nanoparticles: an efficient 3D heterogeneous Electro-Fenton cathode over a wide range of pH 3–9. Environ. Sci. Technol. 50 (10), 5225–5233. https://doi.org/10.1021/acs.est.6b00265.

Zhao, X., Zhang, J.J., Qiao, M., Liu, H.J., Qu, J.H., 2015. Enhanced photoelectrocatalytic decomposition of copper cyanide complexes and simultaneous recovery of copper with a Bi_2MoO_6 electrode under visible light by EDTA/$K_4P_2O_7$. Environ. Sci. Technol. 49 (7), 4567–4574. https://doi.org/10.1021/es5062374.

Zhu, M., Zhang, L.S., Liu, S.S., Wang, D.K., Qin, Y.C., Dai, W.L., Wang, Y.H., Xing, Q.J., Zou, J.P., 2020. Degradation of 4-nitrophenol by electrocatalysis and advanced oxidation processes using Co_3O_4@C anode coupled with simultaneous CO_2 reduction via SnO_2/CC cathode. Chin. Chem. Lett. 31 (7), 1961–1965. https://doi.org/10.1016/j.cclet.2020.01.017.

Zou, J.P., Chen, Y., Liu, S.S., Xing, Q.J., Dong, W.H., Luo, X.B., Dai, W.L., Xiao, X., Luo, J. M., John, C., 2018. Electrochemical oxidation and advanced oxidation processes using a 3D hexagonal Co_3O_4 array anode for 4-nitrophenol decomposition coupled with simultaneous CO_2 conversion to liquid fuels via a flower-like CuO cathode. Water Res. 150, 330–339. https://doi.org/10.1016/j.watres.2018.11.077.